High-speed photography and stress gauge studies of jet impact upon surfaces

N. K. Bourne, T. Obara and J. E. Field

Email alerting service	Receive free email alerts when new articles cite this article - sign up in the box at the top right-hand corner of the article or click **here**

High-speed photography and stress gauge studies of jet impact upon surfaces

By N. K. Bourne[1], T. Obara[2] and J. E. Field[2]

[1]*Shock Physics, Physics and Chemistry of Solids,*
Cavendish Laboratory Department of Physics, Cambridge CB3 0HE, UK
[2]*Department of Mechanical Engineering, Saitama University, Urawa 338, Japan*

Experiments were conducted to investigate the mechanisms of damage to brittle materials by liquid-jet impact as seen in cavitation or simulated rain erosion. In this work, a liquid-jet of 3 mm in diameter and speed *ca.* 600 m s^{-1}, produced using the single-impact jet apparatus (SIJA), was impacted on a polymethylmethacrylate (PMMA) target, chosen as a representative brittle solid. Damage was produced by the liquid jet both near the surface of, and within the bulk of the target. These failure phenomena, which proceeded in several stages, were observed in detail by means of a high-speed camera and with the aid of schlieren visualization techniques. The damage introduced resulted from the interactions of stress waves (compressive, tensile and shear) within the target. A surface ring crack was produced behind a propagating release wave. A central crack along the axis of the jet was also produced by interaction of these waves and, in the case of targets of finite thickness, spall damage was observed at the rear surface. A further crack was opened by the interaction of a shear wave with a reflected release. All the failure mechanisms resulted from wave interactions induced in the target and occurred within a few microseconds of impact.

---

1. Introduction

As is well known, the collision of a high-velocity liquid mass with a solid, generates short high-pressure transients which can cause serious damage to the surface and interior of the target material (see, for example, Bowden & Brunton 1961; Bowden & Field 1964). The problem is significant to a wide range of technologies including rain erosion, cavitation, turbine blade erosion and jet cutting techniques. However, in spite of a considerable amount of research, there remain unexplained and poorly understood phenomena concerning the liquid impact and damage processes. The reasons for this are that the diameter of the liquid drop or jet is generally too small to observe spatial details and the damage takes place over an extremely short period of time of the order of a few microseconds.

Cook (1928) was amongst the first to point out that high pressures can be generated in liquid impact as a result of the so-called 'water-hammer' effect. The water-hammer pressure, P_{WH} for impact on a perfectly rigid target, is given by

$$P_{WH} = \rho c v, \tag{1.1}$$

where ρ and c are the density and shock velocity for the undisturbed liquid, and v the jet impact velocity. This water-hammer pressure lasts (in the case of a cylindrical

Phil. Trans. R. Soc. Lond. A (1997) **355**, 607–623

© 1997 The Royal Society

Printed in Great Britain   607   TEX Paper

jet), for the short period, τ, that it takes a release wave, generated at the contact edge of the jet, to reach the impact axis. This time can be expressed as

$$\tau = \frac{d_{\mathrm{J}}}{2c}, \tag{1.2}$$

where d_{J} is the diameter of the jet. For example, a water-hammer pressure of about 1.5 GPa lasting 1 µs is generated by an impact velocity of 1 km s^{-1} with a jet diameter of 3 mm.

Since most ductile materials have a compressive yield strength below this value, surface pitting is commonly observed in metals and as their tensile strength is much higher, tensile failures around the impact site are not seen (only with thin plates are spall failures seen at the rear surface). In brittle materials, however, the compressive strength is much higher than the tensile strength and so release interactions play a much more important role, as discussed in the case of the circumferential cracking by (Field 1966) where the effect of the Rayleigh surface wave in forming short discrete cracks is demonstrated. In these materials, where the compressive strength is not exceeded, the material in the region beneath the impact itself remains undamaged.

The diameters of the central undamaged surface areas were measured by Bowden & Brunton (1961) and were found to be closely related to the diameter of the jet head. Brunton (1966) investigated the damage pattern observed in 3.5 mm thick polymethylmethacrylate (PMMA) targets and described the three types of damage created, i.e. ring fractures, central on-axis subsurface damage and scabbing near the rear surface of the target. The subsurface shear damage was located at a depth of about half the contact radius. Brunton pointed out that this would be the position of maximum shear as predicted by Hertz (1882) for elastic contact. For such transient loading, this explanation is unlikely to be complete and the present paper suggests a modified damage mechanism. High-speed lateral flow over the circumferential cracks leads to erosion of material since there is a small surface step at each crack. However, flow over an undamaged surface is unlikely to cause further damage except for soft materials such as elastomers (Bowden & Brunton 1961; Field 1967).

Brunton (1966) accounted for the failure mechanism in the solid as due to the short duration of 'explosive' compression and the shear stress generated by the high speed radial flow caused after the jet impact. Field *et al.* (1985) conducted two-dimensional liquid-wedge impacts in order to observe the compression wave and its interaction with an inclined free surface. Their results showed that radial flow is induced by the release wave reflection at the wedge.

Heymann (1969) developed a theoretical treatment for the collision of a liquid sphere on a solid surface in order to investigate the pressure distributions around the impact area. He found that the highest pressure was generated at the contact edge of the liquid jet and that the contact edge pressure progressively decreased from around three times the water-hammer pressure at the edge to the water-hammer pressure on the impact axis. Lesser (1981) also calculated both two and three-dimensional liquid-jet impact taking into account the elasticity of the target material. The result of this analysis also suggested that the edge pressures exceeded the central water-hammer pressure though they are of very short duration. Lush (1983) considered the shape of the jet head and concluded that, for a plane-ended impact, the pressure produced was somewhat in excess of the linear water-hammer pressure because of the increase in liquid bulk modulus. While used to explain the cause of the circumferential crack on these materials, analytical models were unable to explain all the damage modes

found in target materials, in particular the mechanism resulting in the central crack on the liquid-jet axis. While compression wave interactions have been identified as important to the failure mechanics, tensile wave interactions have received much less attention. It is the purpose of this investigation to determine all the mechanisms giving rise to brittle failure modes as a further stimulus to modellers.

A high-speed liquid-jet is also produced within bubbles when they collapse asymmetrically as first suggested by Kornfeld & Sovorov (1944) and experimentally confirmed by Benjamin & Ellis (1966). Many researchers have observed the creation of high-speed liquid microjets in the final stage of the bubble collapse (Naudé & Ellis 1961; Lauterborn & Bolle 1975; Tomita & Shima 1986; Dear & Field 1988; Vogel *et al.* 1989; Bourne & Field 1992, 1994). Naudé & Ellis (1961) also concluded that liquid-jet impact has a major role in the damage processes occurring in many engineering materials. They also found that the diameter of the damage pit produced by shock compression of a bubble on a surface was much smaller than that of the minimum bubble base. Tomita & Shima (1986) conducted a detailed investigation of bubble collapse and damage-pit formation on indium specimens. They concluded that the impulsive pressure, causing plastic deformation of the material, was closely related to the behaviour of the liquid-jet threading a bubble and interacting with the target surface. However, a difficulty arises from the fact that the diameter of the microjet produced in the interior of a bubble is generally too small to observe (cf. one tenth of the initial bubble diameter as shown in the simulations of Plesset & Chapman 1971). Furthermore, it is almost impossible, using conventional optical techniques, to visualize the behaviour of such a microjet at the moment of impact in order to identify the fracture process. These limitations are relaxed by using a two-dimensional analogue (Bourne & Field 1992).

Thus, the present paper describes an experimental investigation into the mechanisms of damage caused by liquid-jet impact, aiming to identify the cause of each damage mode and to describe the failure mechanism using high-speed diagnostics. A liquid-jet of about 3 mm in diameter and with velocity of about 600 m s^{-1} in air was generated by a single-impact jet apparatus (SIJA) and impacted onto the surface of PMMA. Firstly, the waves and damage were visualized using an image converter high-speed camera with the aid of schlieren optics. Additionally, a pressure gauge was constructed and embedded in the target in order to obtain the time dependence of the impact stress. Finally, the damage patterns on and within the recovered target were examined using optical microscopy. A parallel investigation in which liquid jets penetrated water surfaces has recently been described (Bourne *et al.* 1996).

2. Experimental

(*a*) *Single-impact jet apparatus*

Figure 1*a* shows the schematic diagram of the experimental set-up. A vertical liquid jet produced using SIJA (Hand *et al.* 1991) was impacted onto the surface of PMMA. SIJA uses a high pressure reservoir to project a 5.5 mm diameter lead slug down a barrel to impact into a specially-designed stainless steel nozzle (1.6 mm exit orifice diameter). The nozzle was carefully filled with tap water to ensure that there were no bubbles within the chamber and that the meniscus at the end of the exit orifice was convex. When correctly adjusted, the water was extruded from the nozzle at a velocity adjustable between 90 m s^{-1} and 1 km s^{-1} by controlling the reservoir pressure. The impact velocity of the liquid jet was accurately recorded by

610   *N. K. Bourne, T. Obara and J. E. Field*
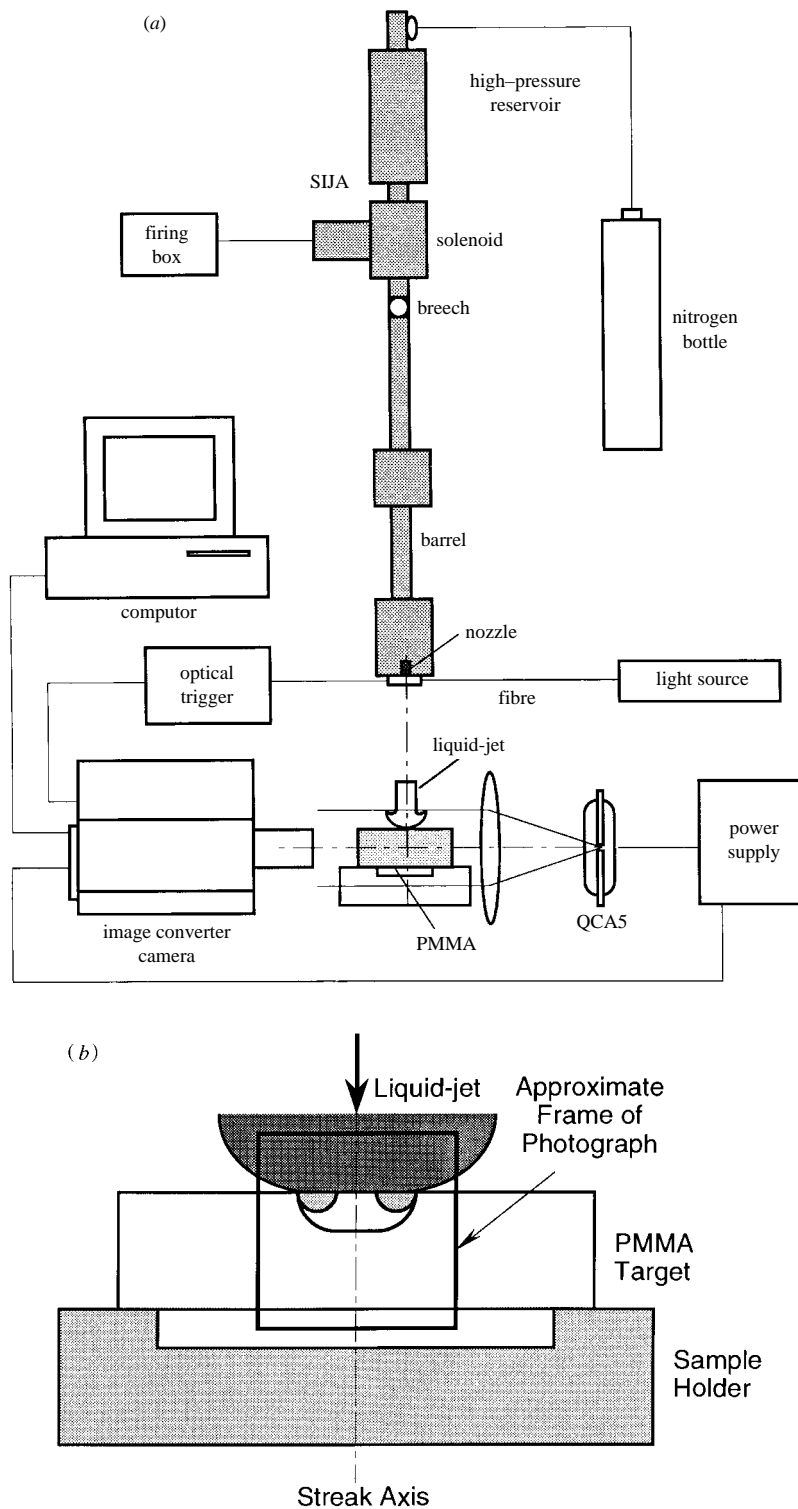
(a)

(b)

Figure 1. (a) Schematic diagram of the experimental set-up. (b) The field of view of the high-speed camera.

electronically measuring the interval taken for the jet to interrupt two light beams. The velocity of the liquid jet used in this experiments was about $600 \, \mathrm{m \, s^{-1}}$ with a firing pressure of 2.0 MPa. The water-hammer pressure at the target surface on the impact axis was estimated, using (1.1) and (1.2), to be around 900 MPa lasting for around $0.5 \, \mu\mathrm{s}$. The experiments were all conducted in air at room temperature, and ambient pressure.

(*b*) *Target material*

PMMA was chosen as a target to observe the details of the stress waves and the fracture process because of its transparency and photoelastic sensitivity. The density, longitudinal and shear wave-speed of PMMA are $1.17 \times 10^3 \, \mathrm{kg \, m^{-3}}$, $2.7 \, \mathrm{km \, s^{-1}}$ and $1.4 \, \mathrm{km \, s^{-1}}$, respectively. Preliminary experiments determined that a distance of 15 mm between the nozzle exit and the surface of the target caused the most severe damage on the PMMA surface since this flight optimized the smooth head of the jet by air ablation. The PMMA sample was $50 \, \mathrm{mm^2}$ and 5.9 or 11 mm thick. The size of the block meant that it was effectively semi-infinite laterally over the time-scale of the impact since compression waves could not reflect from the sides within $7 \, \mu\mathrm{s}$ of impact. Two surfaces of the sample were polished to an optical finish in order to view the compression waves and it was then mounted on a holder perpendicular to the central axis of the jet nozzle. The damage pattern and the structure of the target were observed optically after impact using a low power microscope.

(*c*) *High-speed photography*

The liquid jet impact on the surface of PMMA was photographed by means of an Ultranac FS501 programmable high-speed image converter camera (Imco Electro-Optics). The field of view of the camera was set as shown in figure 1*b* to observe the travel and interaction of waves within the target. The camera was operated in framing or streak mode. The framing rates were varied from 10^6 to 10^7 frames $\mathrm{s^{-1}}$ to observe the detail of the failure mechanisms in the PMMA. In streak mode, the streak axis was accurately aligned with that of the liquid jet. The great advantage of this camera was that the interframe and exposure time for each frame could be adjusted as required using custom software. The sample was mounted in a conventional schlieren system. The flash source was a Xenon (QCA5) tube which delivered 150 J in approximately $100 \, \mu\mathrm{s}$. The camera and the flash source were operated by a delay generator triggered by the liquid jet cutting a light beam at the nozzle exit.

(*d*) *Pressure measurements in the region beneath the impacting liquid-jet*

In order to obtain the time dependence of the impact stress, a pressure gauge was constructed. A polyvinylidene difluoride (PVDF) piezoelectric disc of $25 \, \mu\mathrm{m}$ in thickness was punched to produce a disk of 1.5 mm diameter and connected to brass electrodes of $25 \, \mu\mathrm{m}$ thickness using conductive tape (Scotch 9703 Conductive Adhesive Transfer Tape, 3M). The total thickness of the gauge package was estimated to be about $150 \, \mu\mathrm{m}$. The PVDF gauges were calibrated up to 1 GPa against manganin piezoresistive stress gauges (LM–SS–125CH–048, Measurements Group Inc.) by impacting a flat-ended projectile fired from a single stage gas gun onto a PMMA target with both gauges within (Rosenberg *et al.* 1980). The rise time obtained using the manganin gauge was 20–30 ns while that of the PVDF was around 100 ns due to the greater thickness of the PVDF gauge package. The PVDF was connected in current mode to give the fastest gauge response, i.e. a $51 \, \Omega$ current-viewing resistor
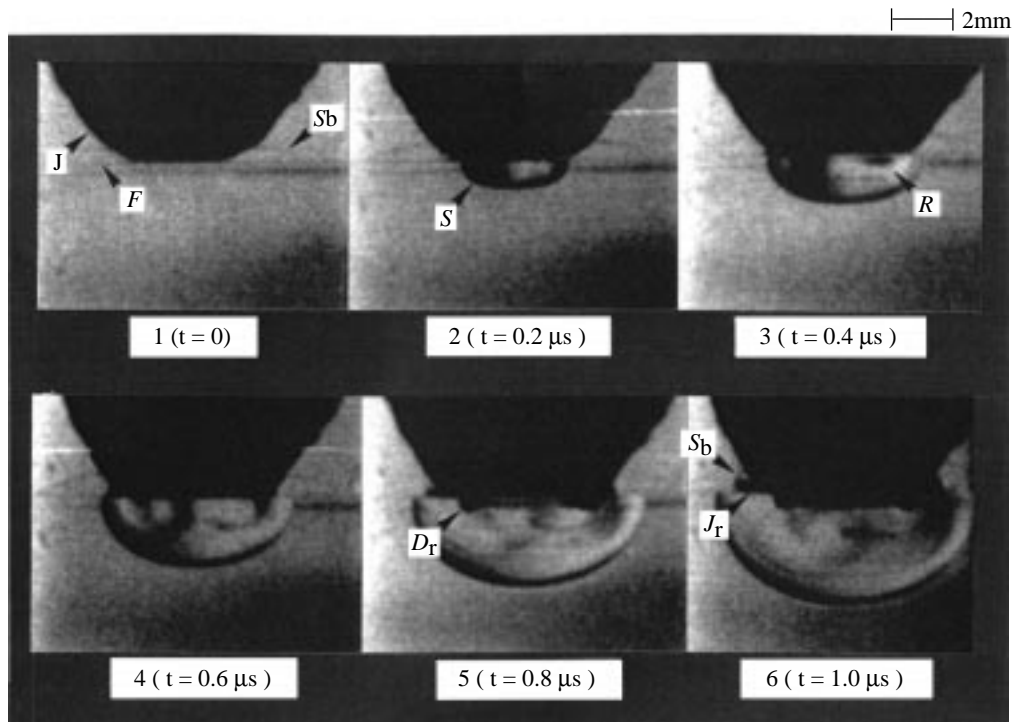
Figure 2. High-speed photograph of the liquid jet impact on the PMMA target. Speed of liquid jet 640 m s^{-1}, interframe time 200 ns, exposure time per frame 40 ns, target thickness 11 mm. F, impact surface; S_b, bow shock wave; J, liquid jet; S, shock wave; R, release wave; D_r, ring crack; J_r, radial jet.

was placed across the gauge and the voltage across it was recorded directly. In this mode the stress derivative was measured and a time integration was carried out numerically to recover the stress signal. The signals from both gauges were recorded by a digital storage oscilloscope (Tektronix, TDS 460). The PVDF gauge was mounted flush with the surface of the PMMA target and held in place by a 25 μm mylar sheet with epoxy resin and the distance between the surface and the gauge was less than 50 μm. Details of the gauge construction, calibration and use can be found in Obara *et al.* (1995).

3. Results and discussion

(*a*) *The behaviour of the liquid jet and the damage*

Figure 2 presents a high-speed sequence (interframe time is 200 ns and exposure time is 40 ns) showing liquid jet impact on a PMMA target of thickness 11 mm. The speed of the jet is 640 m s^{-1} and it enters the frame from above. The impact surface, F, is visible as a horizontal line at the top of each frame. The first frame shows the liquid jet travelling in air before impact and indicates that the front shape of the liquid jet, J, produced by SIJA is not hemispherical but is slightly flattened by aerodynamic ablation (Hand *et al.* 1991). Since the liquid jet has a preceding bow shock, S_b, this reflects from the target before the impact of the jet and this behaviour is visible in frames 1 and 2. Between frame 1 and 2, the liquid jet impacts on the surface of the target and a shock wave, S, is generated which propagates into the
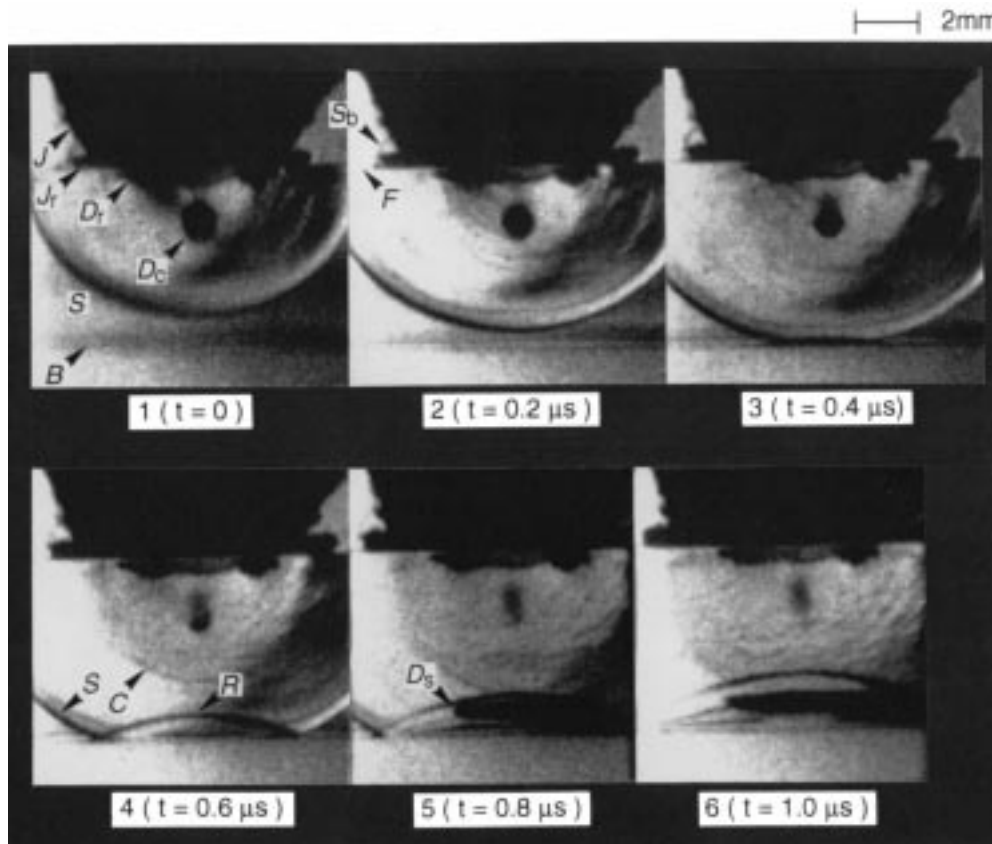
Figure 3. High-speed photograph showing later stage of the liquid jet impact on the PMMA target. Speed of liquid jet 650 m s^{-1}, interframe time 200 ns, exposure time per frame 40 ns, target thickness 5.9 mm. F, impact surface; B, rear surface; J, liquid jet; S, shock wave; S_b, bow shock wave; J_r, radial jet; D_r, ring crack; D_c, central damage; D_s, spalling; R, release wave; C, compression wave.

target. This shock wave has a flat central front associated with the original shape of the liquid jet head. The speed of the shock wave is around 3 km s^{-1} and exceeds the speed of the longitudinal elastic wave in the PMMA. The release waves, R, are visible from frame 3, following the initial shock wave. The radial jet, J_r, is visible from frame 5 onwards, travelling along the surface of the target. Both shock and release waves propagate back into the liquid jet but are not visible due to refraction from the cylindrical surface; however, the release wave reflections at the jet interface may play an important role in the high-speed radial flow as described by Field *et al.* (1985). The velocity of the radial jetting is measured to be about 1.3 km s^{-1}, around twice that of the liquid jet. Further, the radial jets travel on the target surface with a preceding bow shock wave, S_b. This highly accelerated radial jet will produce strong shear on the target surface as suggested by Bowden & Brunton (1961). However the viscous drag force caused by the radial jetting is thought to be too small to initiate damage on the surface of the PMMA target though it can erode material from cracks generated by the Rayleigh surface wave.

From frame 5 onwards, the surface of the target is visibly damaged in a ring, D_r, as
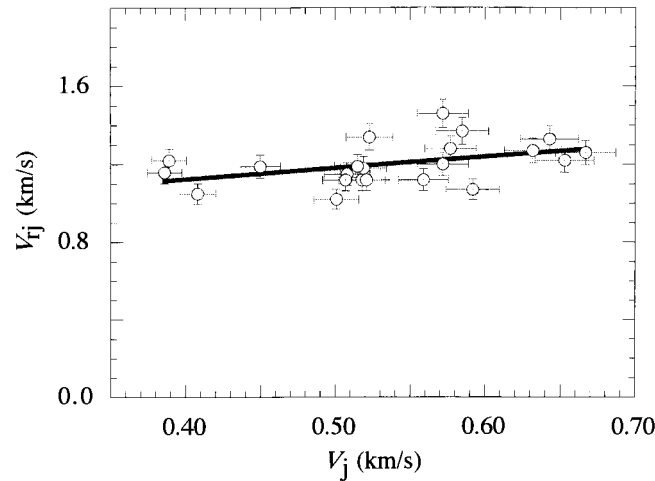
Figure 4. Relationship between the speed of the radial jet and that of the liquid jet: V_{rj}, speed of radial jet; V_{j}, speed of liquid jet.

observed and reported for liquid jet impacts on brittle materials by several authors (Bowden & Brunton 1961; Bowden & Field 1964; Brunton 1966; Field 1966).

Figure 3 shows the impact of a jet onto a finite thickness (5.9 mm) PMMA target. The front, F, and rear surface of the target, B, are seen as parallel lines in each frame. The liquid jet, J, travelling at 650 m s^{-1}, impacts on the upper surface from above. Again the interframe time is 200 ns and the exposure time for each frame is 40 ns. The first frame, 1.7 µs after impact, shows the ring crack, D_{r}. The dark ellipsoidal area on the central axis of the jet is the central damage region, D_{c}, and the mechanism giving rise to it is discussed below. The opened central crack is temporarily closed from above and the damage remains after unloading. The radial jetting, J_{r}, is also present accompanied by the bow shock wave, S_{b}.

The most significant damage occurs near the rear surface from frame 5 onward, as spall damage, D_{s}. The initial shock wave, S, generated by the impact of the liquid jet, reflects as a release fan, R, at the rear surface of the target, B, from frames 3 onwards. When the reflected release wave interacts with a second release generated at the contact edge of the liquid jet, then spalling, D_{S}, starts as seen in frame 5.

This second wave, C, is clearly visible behind the release waves. There are a lot of density variations behind this wave and its speed is equal to the longitudinal wave speed of the PMMA. Further, the opened-up central crack, D_{C}, is closed by interaction with this second wave. The origin of this second wave is effectively the end of the 'water hammer' pulses and the start of the stagnation flow of the liquid jet which gives rise to a pressure P_{ST}, given by

$$P_{\mathrm{ST}} = \tfrac{1}{2}\rho v_{\mathrm{J}}^2, \tag{3.1}$$

where v_{J} is the jet velocity. The stagnation pressure is estimated to be around 200 MPa for this impact.

Figure 4 shows the relationship between the velocity of the surface radial jets and that of the incident jet. It can be seen that the speed of the radial jets is two to three times faster than that of the main jet but that their velocity does not increase strongly with the jet velocity. The damage caused by the radial jet could not be resolved on the flat surface of the target. However, the generation of the high-speed
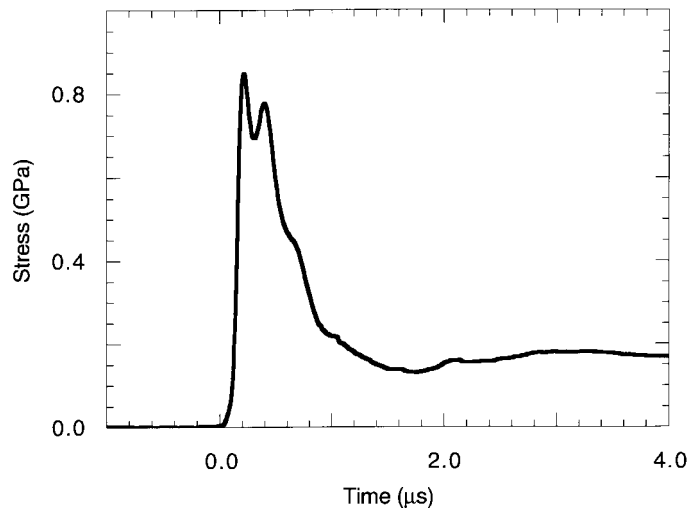
Figure 5. Typical stress signal measured by PVDF pressure gauge. The gauge was mounted on the surface of the target with epoxy resin. Speed of liquid jet 570 m s^{-1}, target thickness 11 mm. The signal of the pressure gauge shows a fast rise time and the peak stress is equivalent to the water-hammer pressure of around 0.85 GPa.

radial jet, as noted above, plays a significant role in propagating the damage on the rough surface where surface asperities are removed, and so becomes particularly important when repeated impacts of the jet (in situations such as rain erosion) are encountered.

(b) *Pressure measurements in the impact zone ahead of the liquid jet*

In earlier studies, pressure measurements of the liquid jet impact were attempted by Bowden & Brunton (1961) using piezoelectric pressure transducers. However, since the sampling rate of their system was several times the duration of the impact, it did not measure the transient impact stress accurately. In their review, Lesser & Field (1983) discuss measurements of the stress distribution around the impact area using piezoelectric ceramic gauges made by various researchers. The data of Rochester (1979) clearly showed high edge pressures. However, this is an area where much more research is required.

Figure 5 shows a typical stress signal measured by a PVDF gauge when a liquid jet of 570 m s^{-1} is impacted on the target surface. The stress signal rises rapidly and reaches a peak of about 0.85 GPa, equivalent to the water-hammer pressure. This stress lasts only 0.5 μs and rapidly falls off. Oscillations on the peak of the trace are typical of this type of gauge and relate to mechanical equilibration of the gauge. The period of the high pressure is also equivalent to the duration calculated by (1.2) assuming that the head diameter of the liquid jet is 3 mm. After the release of the water-hammer stress, the stagnation pressure is applied to the target over a period of around 10 μs after the impact. This stress, of order 200 MPa, is approximately the same amplitude as that calculated using (3.1).

(c) *Fracture mechanisms*

(i) *Ring crack and central damage*

Figure 6 shows a high-speed sequence in which detail of the liquid jet impact and fracture process can be seen. The velocity of the liquid jet is 520 m s^{-1} and
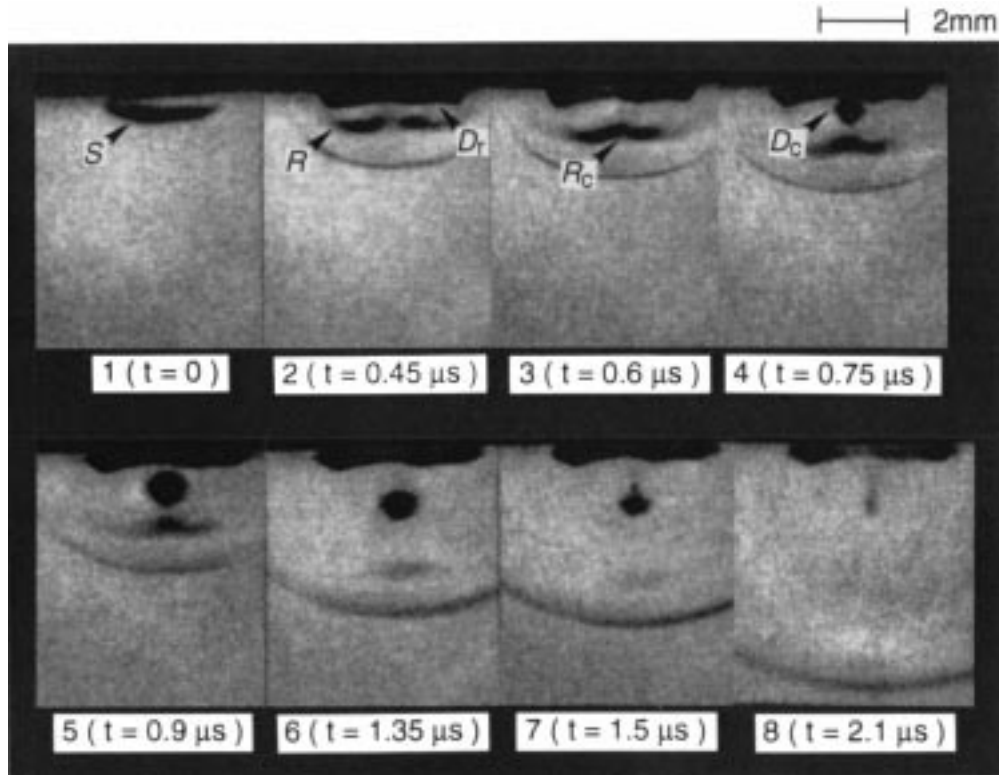
Figure 6. High-speed photograph showing the initiation of the ring crack and the central damage by the release wave. Speed of liquid jet 520 m s^{-1}, target thickness 11 mm, exposure time per frame 50 ns: S, shock wave; R, release wave; D_r, ring crack; R_c, overlapped release wave; D_c, central damage.

the thickness of the target is 11 mm. The exposure time for each frame is 50 ns. The magnification for this photograph is high enough to view the detail of the wave interactions and the processes of failure. In frame 1, the impact shock wave, S, is clearly seen. The release wave, R, is visible from frame 2. The toroidal release wave is generated near the contact edge of the liquid jet because of the large difference of the acoustic impedance at the interface of PMMA and air. In frame 2, a ring crack, D_r, results from the generation of the release waves, perhaps suggesting that the tensile stresses trigger fracture. Bowden & Field (1964) and Field (1966) show that the ring fracture forms at the edge of the loaded area in glasses where high tensile stresses develop during impact around the deformed impact zone. The fracture by this mechanism may be explained by tensile stresses induced around the compressed region beneath the jet.

The release waves overlap three dimensionally near the central axis of the liquid jet, R_C, from frame 3. The central damage crack, D_C, is initiated from frame 4 following the overlap of the release waves, R_C, and grows and migrates downward with time. The shape of the central damage is ellipsoidal but this may merely indicate a region of high strain from which light is refracted, and the major axis is coincident with the direction of release wave propagation. The thickness of the shock wave increases with distance as it travels due to dispersion (Barker & Hollenbach 1970). The central damage appears to close from frame 7 downward by interaction of the compression
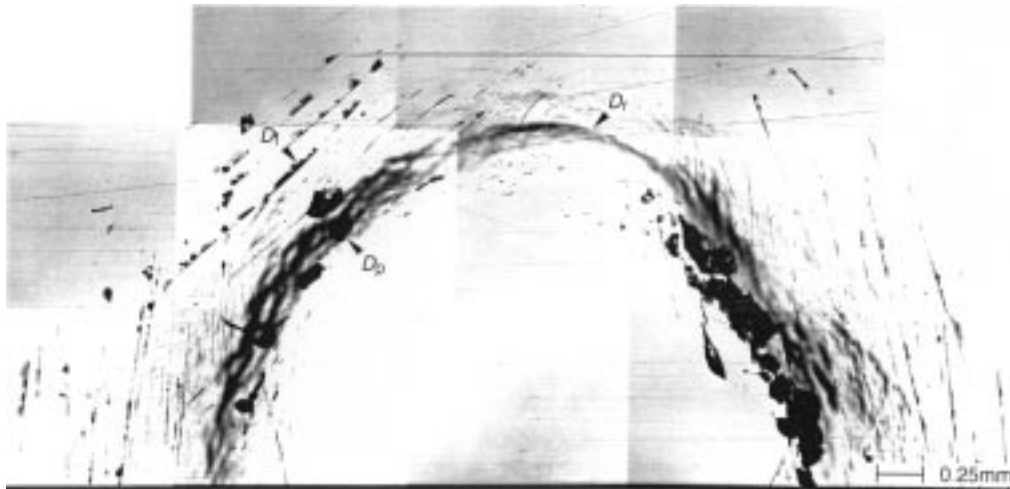
Figure 7. Microscopic observation of the ring fracture on the impact surface: D_r, ring crack; D_p, pits; D_f, short circumferential flaws.

wave associated with stagnation pressure, as shown in figure 3. The ring fracture and the central damage are created by the tensile stresses resulting from the release wave overlap, rather than compression at the contact edge and the shear stress caused by the high-speed radial jet. The distance from the impact face reached by the central crack is determined by the time for which the tensile stresses exceed the spall strength of the target. Since the waves decay with distance, the point at which the crack stops is determined to be that point at which the release amplitude becomes equal to the tensile strength of the material.

Figure 7 presents an optical micrograph of part of the impact surface and shows the structure of the ring crack. The sample was cut into half to observe the damage structure along the central axis. There are several pits, D_P, and circumferential fractures, D_f, on the surface. Not all the ring fractures, D_r, are generated on the surface but some beneath it. The central area inside the ring crack on the impact surface is not damaged at all, even though the water-hammer pressure of around 0.85 GPa is applied in this region. The pits on the surface are caused by the action of the sideways jetting with the circumferential cracking. At higher impact velocities, the ring of damage is very pronounced (Bowden & Brunton 1961). The subsurface ring cracks appear to be caused by the tensile stress generated by the release waves, shown in figure 6. Many short circumferential fractures, D_F, around the ring fracture were initiated by the Rayleigh surface wave at point where flaws or scratches exist as shown by Bowden & Field (1964) and Field (1966).

(ii) *Spallation and middle damage*

Figure 8 is a high-speed photograph showing a later stage of the fracture caused by the liquid jet impact. The exposure time is 50 ns and interframe times are given in the figure. The speed of the liquid jet was 520 m s^{-1} and the thickness of the target was 5.9 mm. The first frame was taken 0.9 µs after the jet impact. The ring crack, D_r, has already been produced by frame 1. The opened-up central crack starts to close from frame 3 onwards and can be seen through the remainder of the sequence and in the recovered sample. The spalling, D_S, starts to develop from frame 5. This spalling, as noted before, is caused by the interaction of two release waves, one produced by
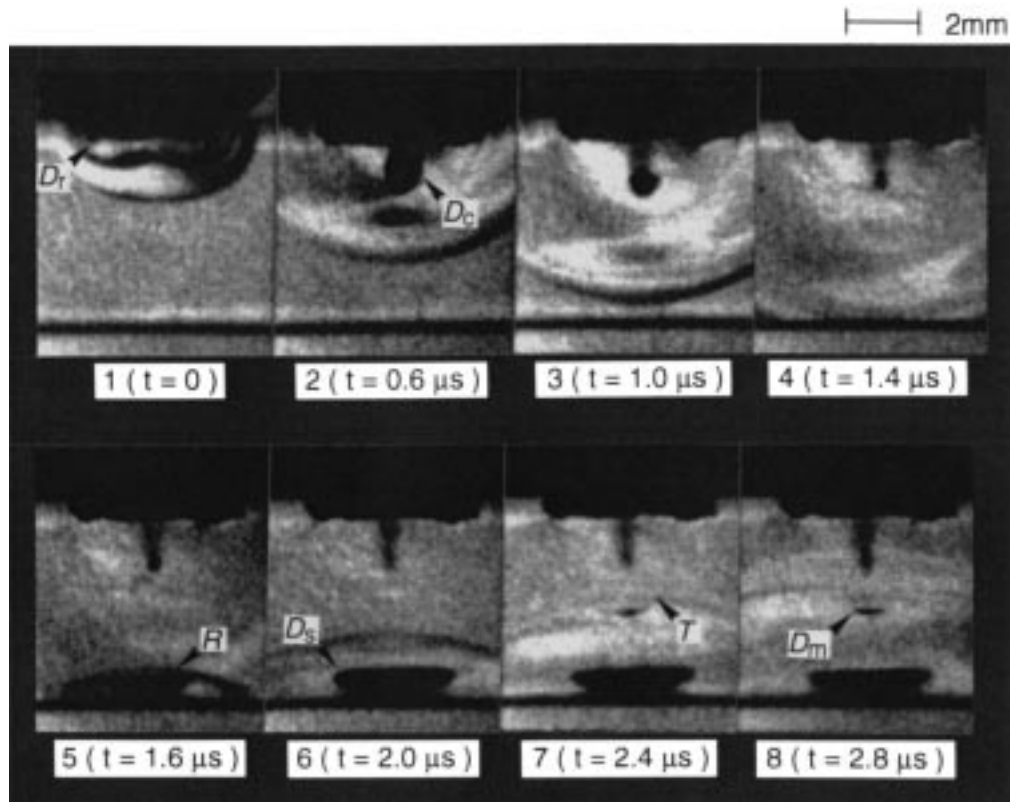
Figure 8. High-speed photograph showing the creation of the spalling near the rear surface and the middle damage. Speed of liquid jet 520 m s^{-1}, exposure time per frame 50 ns, target thickness 5.9 mm: D_r, ring crack; D_c, central damage; D_s, spalling; R, release wave; T, shear wave; D_m, middle damage.

the reflection of the shock wave at the rear surface, R, and the other at the contact edge of the liquid jet, seen in frame 3.

Figure 9 shows a high-magnification photograph of the spall plane near the rear surface. It comprises numerous small penny-shaped cracks with a dark point, D_{SC}, in the centre of each crack. This indicates that these cracks were nucleated and grew from defects. A similar damage structure for polycarbonate has been reported by several authors (Curran *et al.* 1973; Kalthoff & Shockey 1977).

In frame 7 of figure 8, another interesting damage feature is seen in the mid-plane of the target. This middle damage, D_m, is generated beneath the central crack and has been found consistently under these experimental conditions. From frame 5, the release wave, R, which is caused by the reflection of the impact shock wave, propagates from the rear surface upwards, while a spherical wave, T, originating near the tip of the central damage, is clearly visible in frame 7 after the central crack closes. The release wave interacts with this spherical wave damaging the middle portion of the target. Therefore, the damage found in the middle portion is a consequence of fracture and wave interactions.

Figure 10 shows a streak picture in which the horizontal axis indicates the time and the vertical axis the position along the central axis of the liquid jet. The temporal and spatial scale bars are shown in the figure. The thickness of the target is 5.9 mm and the impact surface, F, and rear, B, of the PMMA target are visible as horizontal
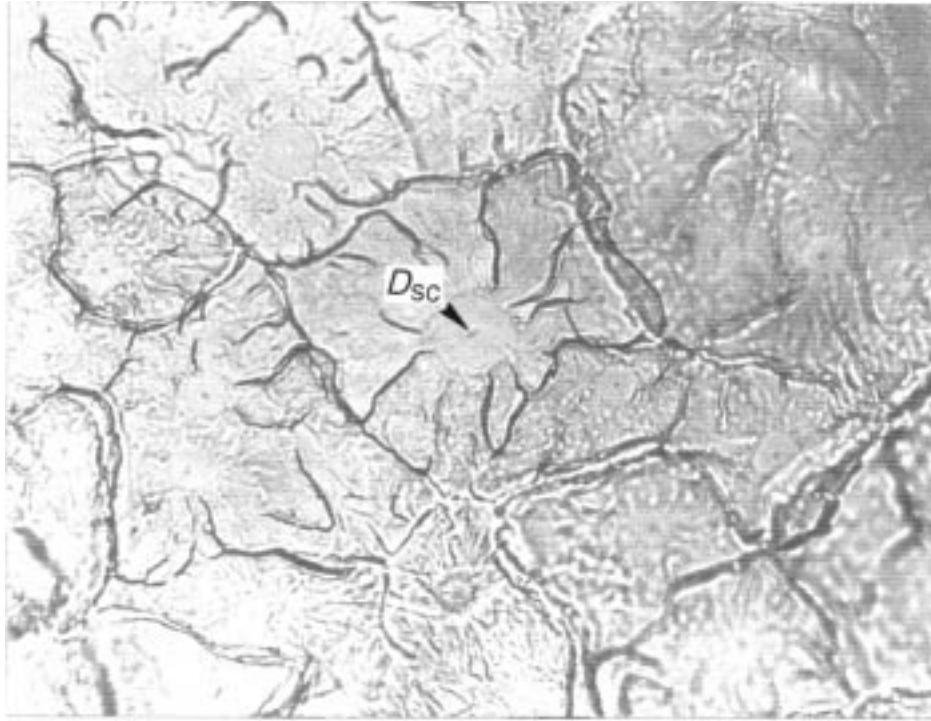
Figure 9. Microscopic observation of the spall plane. The spall plane is constructed from many small penny-shaped cracks: D_{sc}, centre (initial flaw site) of the crack.
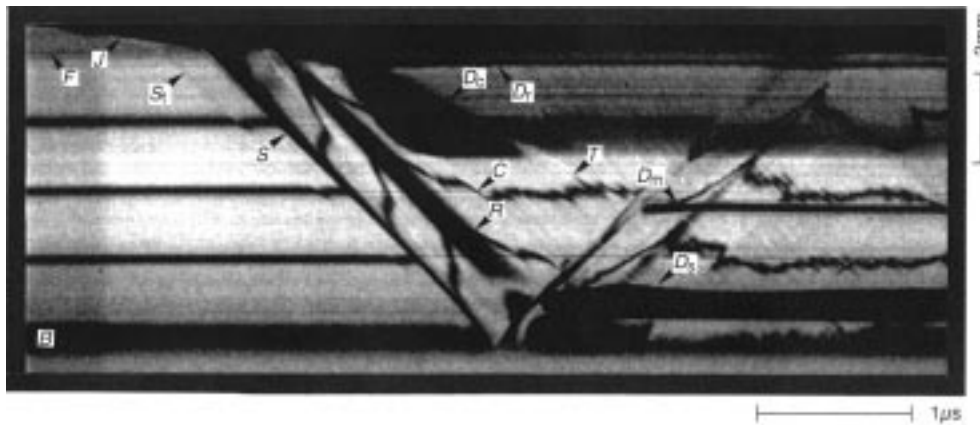

Figure 10. Streak picture showing the details of the liquid jet impact and the fracture process. Speed of liquid jet 580 m s^{-1}, target thickness 5.9 mm: F, impact surface; B, rear surface; J, liquid jet; S_t, transmitted bow shock wave; S, shock wave; R, release wave; D_r, ring crack; D_c, central damage; D_s, spalling; C, compression wave; T, shear wave; D_m, middle damage.

lines. The three horizontal lines between two surfaces are marker lines at a spacing of 1.5 mm starting from the impact surface. The lines are ruled on the distant polished face of the target as viewed from the camera so that they are seen *through* the wave structure after impact. Thus each wave can be identified as either a compression or a tensile wave by the different direction in which the line shifts as light is refracted by the wave. Downward shifts in the figure indicate compression whereas upward

movement indicates release. The speed of the liquid jet is 580 m s^{-1} and the jet, J, is visible at the left hand side of the figure, travelling downward. The bow shock wave travelling ahead of the jet in air, is also clearly observable and transmitted into the target material as S_t. The speed of this transmitted shock wave is equal to the longitudinal wave speed of the PMMA. The shift direction of the three marker lines behind this shock wave is downward across the shock front. The magnitude of the shift is quite small indicating the weakness of the bow shock wave. However, the shock wave, S, generated by the liquid jet impact is clearly visible and the line shift is quite large. The overlapped release waves, R, can be seen travelling behind the shock wave and catching it from the rear. The line shift direction is the reverse of that for the shock wave. The ring cracks, D_r, on the surface are generated behind the release waves and appear as a dark region. Eventually, the central damage crack, D_C, initiates following the overlapping of the release fans. The spalling, D_S, develops when the two release fans interact with each other around 1 mm from the rear surface. The compression wave, C, associated with the stagnation pressure, can also be seen to start to close the central crack region. Note the small magnitude of the wave in comparison with the main shock. It can be seen that another wave, T, is produced which defines the rear of the black region corresponding to the central damage and propagates downward to interact with the reflected release, R. The middle damage, D_m, is caused just after the interaction of these two waves. The speeds of the impact shock wave and release waves are around 2.7 km s^{-1} and 3.2 km s^{-1}, respectively. However, the speed of the wave, T, originating from the closing of the central damage, is slower travelling at 1.4 km s^{-1}, i.e. equivalent to the speed of a shear wave in PMMA. Furthermore, the line shift associated with this wave is almost negligible which further suggests that no large volumetric strain is associated with it. Thus, this wave, T, is a shear wave, and is associated with the closure of the central damage feature.

Figure 11 is a through-thickness view of a sectioned target of 5.9 mm thickness. The ring crack, D_r, can be seen beneath the surface while occasional pits, D_P, can be observed on it. The central damage region, D_C, consists of many microcracks aligned along the hemispherical fronts of the propagating release fronts. These could be caused by the tensile stresses behind the overlapping release waves, as shown in figure 6. The middle damage, D_m, is visible below the central damage and on the central axis of the jet. It appears to be similar to the spall region D_S seen at the rear of the target.

4. Conclusions

Liquid jets were impacted on the surfaces of PMMA targets to investigate the damage mechanisms induced in brittle materials and associated with rain erosion and cavitation damage. The wave interactions and fracture processes of the target were visualized using an image converter high-speed camera and schlieren optics. The fundamental failure modes induced by the liquid jet impact are summarized as follows.

Circumferential ring cracks were generated at the impact surface by the strong tensile stresses generated by the impact. The release waves overlapped on the central axis generating tensile failure. In the case of relatively thin targets, spall fracture was generated by the interaction of release waves. The middle portion of the target was also damaged by the interaction of the release and a shear wave generated by the
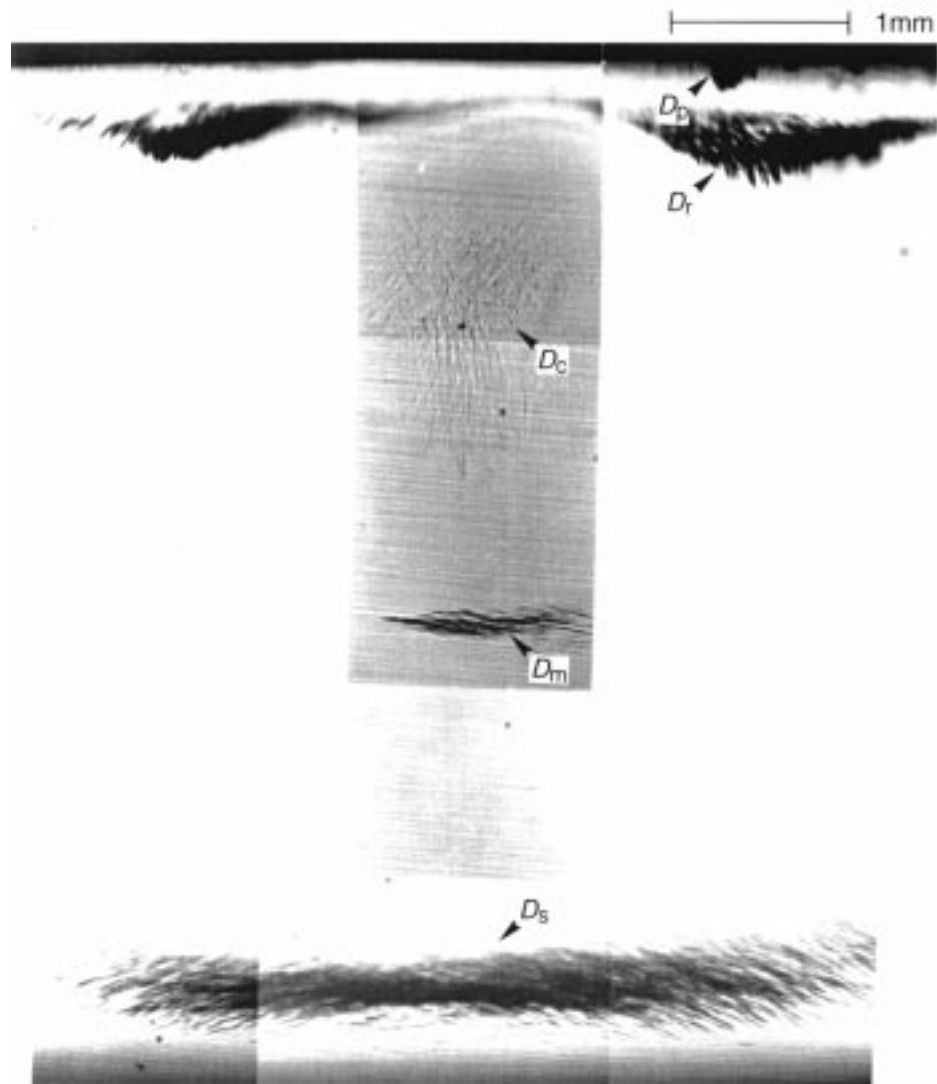
Figure 11. Microscopic observation of the damage. Side view of cross section along the central axis. Target thickness, 5.9 mm: D_p, pits; D_r, ring crack; D_c, central damage; D_m, middle damage; D_s, spalling.

closure of the subsurface failure. Thus, four distinct failure mechanisms operated in the target in response to the stress wave loading experienced by the material. The PVDF gauges confirmed the magnitude and stresses predicted from the theory. Nonetheless this is an area where further research, both experimental and theoretical is needed.

622   *N. K. Bourne, T. Obara and J. E. Field*

References

Barker, L. M. & Hollenbach, R. E. 1970 Shock-wave studies of PMMA, fused silica, and sapphire. *J. Appl. Phys.* **41**, 4208–4226.

Benjamin, T. B. & Ellis, A. T. 1966 The collapse of cavitation bubbles and the pressures thereby produced against solid boundaries. *Phil. Trans. R. Soc. Lond.* A **260**, 221–240.

Bourne, N. K. & Field, J. E. 1992 Shock-induced collapse of single cavities in liquids. *J. Fluid Mech.* **244**, 225–240.

Bourne, N. K. & Field, J. E. 1994 Cavity collapse in a liquid with solid particles. *J. Fluid Mech.* **259**, 149–165.

Bourne, N. K., Obara, T. & Field, J. E. 1996 The impact and penetration of a water surface by a liquid jet. *Proc. R. Soc. Lond.* A **452**, 1497–1502.

Bowden, F. P. & Brunton, J. H. 1961 The deformation of solids by liquid impact at supersonic speeds. *Proc. R. Soc. Lond.* A **263**, 433–450.

Bowden, F. P. & Field, J. E. 1964 The brittle fracture of solids by liquid impact, by solid impact, and by shock. *Proc. R. Soc. Lond.* A **282**, 331–352.

Brunton, J. H. 1966 High speed liquid impact. *Phil. Trans. R. Soc. Lond.* A **260**, 79–85.

Cook, S. S. 1928 Erosion by water-hammer. *Proc. R. Soc. Lond.* A **119**, 481–488.

Curran, D. R., Shockey, D. A. & Seaman, L. 1973 Dynamic fracture criteria for a polycarbonate. *J. Appl. Phys.* **44**, 4025–4038.

Dear, J. P. & Field, J. E. 1988 A study of the collapse of arrays of cavities. *J. Fluid Mech.* **190**, 409–425.

Field, J. E. 1966 Stress waves, deformation and fracture caused by liquid impact. *Phil. Trans. R. Soc. Lond.* A **260**, 86–93.

Field, J. E. 1967 The importance of surface topography on erosion damage. *Proc. 2nd Intl. Conf. on Erosion and associated phenomena* (ed. A. A. Fyall & R. B. King), pp. 593–603. Farnborough: RAE.

Field, J. E., Lesser, M. B. & Dear, J. P. 1985 Studies of two-dimensional liquid-wedge impact and their relevance to liquid-drop impact problems. *Proc. R. Soc. Lond.* A **401**, 225–249.

Hand, R. J., Field, J. E. & Townsend, D. 1991 The use of liquid jets to simulate angled drop impact. *J. Appl. Phys.* **70**, 7111–7118.

Hertz, H. 1882 Über die Berührung fester elastiche Körper and über die Harte. In *Verhandlungen des Vereins zur Beförderung des Gewerbefleisses*. Leipzig. (Engl. Transl. 1896 On the contact of elastic solids. In *Miscellaneous papers by H. Hertz* (ed. Jones & Schott). London: MacMillan.)

Heymann, F. J. 1969 High-speed impact between a liquid drop and a solid surface. *J. Appl. Phys.* **40**, 5113–5122.

Kalthoff, J. F. & Shockey, D. A. 1977 Instability of cracks under impulse loads. *J. Appl. Phys.* **48**, 986–993.

Kornfeld, M. & Sovorov, L. 1944 On the destructive action of cavitation. *J. Appl. Phys.* **15**, 495–506.

Lauterborn, W. & Bolle, H. 1975 Experimental investigations of cavitation-bubble collapse in the neighbourhood of a solid boundary. *J. Fluid Mech.* **72**, 391–399.

Lesser, M. B. 1981 Analytic solutions of liquid-drop impact problems. *Proc. R. Soc. Lond.* A **377**, 289–308.

Lesser, M. B. & Field, J. E. 1983 The impact of compressible liquids. *A. Rev. Fluid Mech.* **15**, 97–122.

Lush, P. A. 1983 Impact of a liquid mass on a perfectly plastic solid. *J. Fluid Mech.* **135**, 373–387.

Naudé, C. F. & Ellis, A. T. 1961 On the mechanism of cavitation damage by nonhemispherical cavities collapsing in contact with solid boundaries. *Trans. ASME D: Jl Basic Engng* **83**, 648–656.

Obara, T., Bourne, N. K. & Mebar, Y. 1995 The construction and calibration of an inexpensive PVDF stress gauge for fast pressure measurements. *Meas. Sci. Technol.* **6**, 345–348.

Plesset, M. & Chapman, R. 1971 Collapse of an initially spherical vapour cavity in the neighbourhood of a solid boundary. *J. Fluid Mech.* **47**, 283–290.

Rochester, M. C. 1979 The impact of a liquid drop and the effect of liquid properties on erosion. Ph.D. thesis, University of Cambridge.

Rosenberg, Z., Yaziv, D. & Partom, Y. 1980 Calibration of foil-like manganin gauges in planar shock wave experiments. *J. Appl. Phys.* **51**, 3702–3705.

Tomita, Y. & Shima, A. 1986 Mechanisms of impulsive pressure generation and damage pit formation by bubble collapse. *J. Fluid Mech.* **169**, 535–564.

Vogel, A., Lauterborn, W. & Timm, R. 1989 Optical and acoustic investigations of the dynamics of laser-produced cavitation bubbles near a solid boundary. *J. Fluid Mech.* **206**, 299–338.